Dynamics of photoionization of hydrogenlike ions in Debye plasmas

Y. Y. Qi,[1,2] J. G. Wang,[2] and R. K. Janev[3]
[1]*School of Electrical Engineering, Jiaxing University, Jiaxing 314001, China*
[2]*Laboratory of Computational Physics, Institute of Applied Physics and Computational Mathematics, P.O. Box 8009-26, Beijing 100088, China*
[3]*Macedonian Academy of Sciences and Arts, P.O. Box 428, 1000 Skopje, Macedonia*
(Received 22 July 2009; published 2 December 2009)

Photoionization processes for the ground state and $n \leq 3$ excited states of hydrogenlike ions embedded in a weakly coupled plasma are investigated in the entire energy range of a nonrelativistic regime. The plasma screening of the Coulomb interaction between charged particles is described by the Debye-Hückel model. The energy levels and wave functions for both the bound and continuum states are calculated by solving the Schrödinger equation numerically by the symplectic integrator. The screening of Coulomb interactions reduces the number of bound electron states, decreases their binding energies, broadens the radial distribution of electron wave functions of these states, and changes significantly the phases and the amplitudes of continuum wave functions. These changes strongly affect the dipole matrix elements between the bound and continuum states and, hence, the photoionization cross sections. The most significant effects of the screened Coulomb interactions on the energy behavior of photoionization cross sections are manifested in its low-energy behavior (Wigner threshold law), the appearance of multiple shape and virtual-state resonances when the energy levels of upper bound states enter the continuum after certain critical strength of the screening, and in the (slight) reduction of the cross section at high photon energies. All these features of the photoionization cross section are related to the short-range character of the Debye-Hückel potential. The effects of the potential screening on the Combet-Farnoux and Cooper minima in the photoionization cross section are also investigated. Comparison of calculated photoionization cross sections with the results of other authors, when available, is made.

DOI: 10.1103/PhysRevA.80.063404 PACS number(s): 32.80.Fb, 52.20.−j

I. INTRODUCTION

The effects of screened Coulomb interaction between charged particles in hot dense plasmas on the structure and collision properties of atomic species have been subject to numerous studies in the last 30–40 years (see, e.g., [1–3] and references therein). These studies have been motivated mainly by the research in laser produced plasmas, extreme ultraviolet and x-ray laser development, inertial confinement fusion, and astrophysics (stellar atmospheres and interiors). The densities (n) and temperatures (T) in these plasmas span the ranges $n \sim 10^{15}-10^{18}$ cm^{-3}, $T \sim 0.5-5$ eV (stellar atmospheres), $n \sim 10^{19}-10^{21}$ cm^{-3}, $T \sim 50-300$ eV (laser produced plasmas), and $n \sim 10^{22}-10^{26}$ cm^{-3}, $T \sim 0.5-10$ keV (inertial confinement fusion plasmas). The Coulomb interaction screening in these plasmas is a collective effect of the correlated many-particle interactions, and to the lowest particle correlation order (pairwise correlations) it reduces to the Debye-Hückel potential (for the interaction of an ion of charge Z with an electron) [1–3],

$$V(r) = -\frac{Ze^2}{r}\exp\left(-\frac{r}{D}\right), \tag{1}$$

where $D=(k_B T_e/4\pi e^2 n_e)^{1/2}$ is the Debye screening length, T_e and n_e are the plasma electron temperature and density, respectively, and k_B is the Boltzmann constant. The representation of charged particle interaction in a plasma by the potential [Eq. (1)] is adequate only if the Coulomb coupling parameter $\Gamma = e^2/(ak_B T_e)$ and plasma nonideality parameter $\gamma = e^2/(Dk_B T_e)$ satisfy the conditions $\Gamma \leq 1$, $\gamma \ll 1$, where $a = [3/(4\pi n_e)]^{1/3}$ is the average interparticle distance. There is a wide class of laboratory and astrophysical plasmas in which these conditions are fulfilled (Debye plasmas). Expressions for the screened Coulomb interaction for strongly coupled and nonideal plasmas can be found elsewhere (see, e.g., [1,2]).

The photoionization process is one of the major factors determining the opacity of stellar objects where it usually takes place in a plasma environment. It is also a very important process in laser produced and inertial confinement plasmas taking part in the ionization and energy balance, as well as in the level population kinetics of plasma atomic species. The plasma effects on the photoionization process have been studied in the past under various assumptions about the form of the screening defined by the plasma conditions (see [1,2] for references). Studies of this process in a Debye plasma were reported in [4–10], the most elaborate of them being those in [8–10]. In [4–6], the wave functions of the bound and continuum electrons were determined by numerically solving the Schrödinger equation with the potential [Eq. (1)] but only for a limited number of screening lengths. The emphasis in these studies was placed mainly on the threshold energy region where the Wigner threshold law behavior [11] was demonstrated and on the appearance of shape resonances in the cross section [5]. In Ref. [7] the Born approximation was employed to calculate photoionization cross section for a number of screening lengths. This approximation is obviously inadequate for describing the photoionization dynamics except at very high energies. In [8–10] the complex-coordinate rotation method was used to calculate the photoionization cross section for a number of screening lengths. As in [4–6], the selection of screening lengths in these papers was guided by the objective to demonstrate the

main effect of the interaction screening on the cross section: its drastic reduction in the near-threshold energy region with respect to the pure Coulomb case. In Ref. [8] the photoionization of H and He^+ was studied, in [9] the photoionization of Li and Na atoms was considered within the one-electron approximation (with a suitable model potential), while in [10] the photoionization of $He(1s2s;{}^1S)$ and $He(1s2p;{}^1P)$ was investigated. The lack of a systematic investigation in all these papers of the detailed behavior of bound-state energies near the ionization continuum has resulted in overlooking important aspects of the photoionization dynamics of hydrogenlike ions in a Debye plasma. Thus, in Ref. [5], while the physical basis for the appearance of near-threshold shape resonances in photoionization cross section was clearly elucidated (as transitions to quasibound states with nonzero angular momentum supported by the centrifugal barrier in the potential), no relation was established between their appearance and the critical strength of the screening at which a particular bound state enters the continuum. In Ref. [5] also the effects of near-zero-energy (virtual) s states on the cross section for $np \rightarrow \varepsilon s$ transitions were discussed, but, again, no relation between the appearance of these states and the screening parameter was established. In Ref. [8], sharp near-threshold peaks in the photoionization cross sections for certain values of the screening were observed, but they were not associated with the shape resonances. Cooper minima [12–14] were observed in Ref. [9] in the photoionization cross sections for Li and Na in Debye plasmas. However, since the problem was treated in one-electron approximation and the active electron interaction with the ionic core was represented by a model potential containing terms similar to that of Eq. (1) there remains an ambiguity regarding the origin of the observed Cooper minima. The Combet-Farnoux minima [15,16], which are also a specific feature of the photoionization cross section in the plasma free case, have not been observed in either of the mentioned studies with a Debye-Hückel potential.

In the present paper we shall try to present the full picture of the photoionization dynamics in hydrogenlike ions in the states with principal quantum number $n \leq 3$ embedded in a Debye plasma by choosing appropriately the values of Debye screening length. As the near-threshold behavior of the cross section has already been studied in detail in [4–10], we shall focus our attention on the other specific features of the photoionization cross section: the shape resonances, the Cooper and Combet-Farnoux minima, and the broad near-threshold resonances due to the appearance of virtual s states. We should note that the shape and virtual-state resonances, as well as the Cooper minima, do not appear in the photoionization of hydrogenlike ions with a pure Coulomb interaction [17,18] and can, therefore, be considered as specific manifestations of the short-range screened Coulomb interaction. A rigorous proof of the nonexistence of Combet-Farnoux minima in hydrogenlike systems with pure Coulomb interaction is not known to the present authors. However, the photoionization cross sections from $1s$, $2l$, and $3l$ Coulomb bound states, calculated in the present work for comparison purposes with the screened case, indicate absence of Combet-Farnoux minima in the photoionization cross section of isolated hydrogenlike systems.

We should also mention that the appearance of shape resonances and Cooper minima in the photoionization of isolated many-electron atomic systems, treated in the independent particle approximation, has always been associated with the nuclear screening by the "passive" electrons and with the appearance of a centrifugal barrier in the effective potential for the nonzero angular momentum continuum states (see, e.g., [19–22] and references therein). However, the effective one-particle potential in many-electron atomic systems depends on their specific electronic structure and does not provide a smoothly varying screening parameter for establishing a transparent correlation between the photoionization dynamics and the Coulomb interaction screening. The potential [Eq. (1)] does provide such a parameter, the Debye length D. There is another important difference between the interaction screening in the isolated many-electron atoms (or ions) and the screened Debye-Hückel potential [Eq. (1)]. While in the former case the interaction screening experienced by the "active" electron is restricted in the radial regions associated with the dominant electron density distribution in the atom (ion) (and, thus, in the asymptotic region the interaction retains its Coulomb character), in the latter case the interaction screening extends to infinity. This circumstance will obviously produce certain differences in the photoionization dynamics of these two physical cases, as we shall see later in this work.

For determination of the bound and continuum state electron wave functions in the Debye-Hückel potential [Eq. (1)] we have employed the fourth-stage fourth-order symplectic integration scheme [23,24] to solve numerically the radial Schrödinger equation. This numerical method provides a high computational accuracy for both the bound-state energies and bound and continuum electron wave functions (see Sec. II). We mention that this method has already been applied in our previous studies of bound-bound transitions [23], electron-impact excitation [26] of hydrogenlike ions, and photoionization of the ground state and excited Li atom (treated in the one-electron approximation) [27] in Debye plasmas.

The paper is organized as follows. In Sec. II we briefly describe the method of wave function calculations and analyze the wave function and bound-state energy behavior as the interaction screening varies. In Sec. III we present the results of our photoionization cross section calculations and discuss the relation of characteristic cross section features with the strength of the interaction screening. In Sec. IV we give our conclusions.

Atomic units will be used in the remaining part of this work unless otherwise explicitly stated.

II. COMPUTATIONAL METHOD, WAVE FUNCTIONS, AND BOUND-STATE ENERGIES

A. Computational method

The radial Schrödinger equation for a hydrogenlike ion with nuclear charge Z in a Debye plasma is given by

$$\left(-\frac{d^2}{2dr^2}+\frac{l(l+1)}{2r^2}+V(r)\right)P_{\kappa l}(r;Z,D)=E_{\kappa l}(Z,D)P_{\kappa l}(r;Z,D), \tag{2}$$

where $P_{\kappa l}(r;Z,D)$ is the radial electron wave function, $\kappa=n$ for the discrete states (the principal quantum number) and $\kappa=k(=\sqrt{2\varepsilon})$ for the continuum states (the wave number of continuum electron with energy ε), l is the angular quantum number, and the potential $V(r)$ is given by Eq. (1) (with $e^2=1$).

By making the scaling transformations

$$\rho=Zr, \quad \delta=ZD, \quad \varepsilon_{\kappa l}(\delta)=E_{\kappa l}(Z,D)/Z^2. \tag{3}$$

Equation (2) is reduced to the form

$$\left(-\frac{d^2}{2d\rho^2}+\frac{l(l+1)}{2\rho^2}-\frac{\exp(-\rho/\delta)}{\rho}\right)P_{\kappa l}(\rho;\delta)=\varepsilon_{\kappa l}(\delta)P_{\kappa l}(\rho;\delta), \tag{4}$$

which is the radial Schrödinger equation for the hydrogen atom in the scaled units. The bound-state radial wave functions are normalized in the standard way,

$$\int_0^\infty d\rho P_{nl}(\rho;\delta)P_{n'l}(\rho;\delta)=\delta_{n,n'}, \tag{5}$$

while the continuum wave functions are normalized to unit energy interval [28],

$$\int_0^\infty d\rho P_{\varepsilon l}(\rho;\delta)\int_{\varepsilon-\Delta\varepsilon}^{\varepsilon+\Delta\varepsilon}P_{\varepsilon' l}(\rho;\delta)d\varepsilon'=1, \tag{6}$$

where $\Delta\varepsilon$ is a small energy interval.

For the short-range potential [Eq. (1)], the asymptotic behavior of the continuum radial wave function has the form [29]

$$P_{\varepsilon l}(\rho;\delta)\sim A(k\rho j_l(k\rho))-B(k\rho n_l(k\rho)) \cong C\left[\sin\left(k\rho-\frac{l\pi}{2}\right)+\tan\Delta_l\cos\left(k\rho-\frac{l\pi}{2}\right)\right], \tag{7}$$

where $j_l(k\rho)$ and $n_l(k\rho)$ are the spherical Bessel and Neumann functions, respectively, and Δ_l is the phase shift of the lth partial wave in the potential [Eq. (1)]. The phase shifts Δ_l can be evaluated by the following formula [29]:

$$\tan\Delta_l=\frac{P_{\varepsilon l}(\rho_b;\delta)S(\rho_a)-P_{\varepsilon l}(\rho_a;\delta)S(\rho_b)}{P_{\varepsilon l}(\rho_a;\delta)C(\rho_b)-P_{\varepsilon l}(\rho_b;\delta)C(\rho_a)}, \tag{8}$$

where ρ_a and ρ_b are two distinct points in the asymptotic region such that for $\rho>\rho_m$ $S(\rho)=k\rho j_l(k\rho)\cong\sin(k\rho-\frac{l\pi}{2})$ and $C(\rho)=-k\rho n_l(k\rho)\cong\cos(k\rho-\frac{l\pi}{2})$. The maximum and minimum (negative maximum) amplitude values, $A_{\max}$ and $A_{\min}$, of the oscillating wave functions in the asymptotic region should be equal, so that we can find ρ_m by an iterative procedure and make the condition

$$|A_{\max}+A_{\min}|<\xi_1, \quad \rho>\rho_m \tag{9}$$

to be satisfied, where ξ_1 is sufficiently small and defined by the requirement on the computational accuracy. Similarly, any two phase shifts, Δ_{l1} and Δ_{l2}, for the same partial wave l should be equal in the asymptotic region, which imposes the condition

$$|\Delta_{l1}-\Delta_{l2}|<\xi_2, \quad \rho>\rho_m, \tag{10}$$

where ξ_2 has the same meaning as ξ_1. When the conditions [Eqs. (9) and (10)] are satisfied simultaneously, the normalized continuum wave function is given by

$$P_{\varepsilon l}(\rho;\delta)=\frac{1}{2^{1/4}\pi^{1/2}\varepsilon^{1/4}}\frac{P^u_{\varepsilon l}(\rho;\delta)}{A_{\max}}, \tag{11}$$

where $P^u_{\varepsilon l}$ is the un-normalized continuum wave function computed numerically.

The normalized continuum wave function has dimension $(\text{energy})^{1/2}$, so that the continuum wave function of hydrogenlike ion with nuclear charge Z is scaled as

$$P_{El}(r;Z,D)=Z^{-1/2}P_{\varepsilon l}(\rho;\delta). \tag{12}$$

We have solved Eq. (4) for the discrete and continuous spectrum by employing the fourth-stage fourth-order symplectic integration scheme. The technical details of the method are described in detail elsewhere [25,26] and we refrain of repeating them here. We only note that the accuracies provided by this method in its implementation in the present work are 10^{-7} for the energies and 10^{-5} for the wave functions. A similar level of accuracy in solving numerically Eq. (4) has been achieved in Ref. [30].

B. Basic properties of energies and wave functions of Debye-Hückel potential

1. Critical screening lengths and quasibound and near-zero-energy states

As it is well known (see, e.g., [31]), the potential [Eq. (1)], which decreases with increasing r faster than $-1/r^2$, supports only a finite number of bound states for any finite value of D. Moreover, the l degeneracy of the energy levels, characteristic for the pure Coulomb potential, is lifted in the screened Coulomb potential [Eq. (1)]. The finite number of bound states for any finite value of D implies that with decreasing D the electron binding energy decreases and at a certain critical value D^c_{nl} it becomes zero. In Fig. 1 we show the scaled energies ε_{nl} of the $1s$, $2l$, and $3l$ states as a function of the scaled screening length $\delta=ZD$. The figure shows that with decreasing δ the scaled energies rapidly approach the continuum edge. The critical scaled Debye lengths, $\delta^c_{nl}=ZD^c_{nl}$, where $\varepsilon_{nl}(\delta^c_{nl})=0$, are given in Table I for all the states with $n\leq 6$. They are compared with the values obtained in Ref. [30]. There is an excellent agreement between the two sets of data. As we shall see later, the critical screening lengths play a crucial role in the appearance of the characteristic features of the photoionization cross section: the shape and virtual-state resonances and the Cooper minima.

For the states with angular momentum $l>0$ the effective radial potential in the Schrödinger equation [Eq. (2)] is

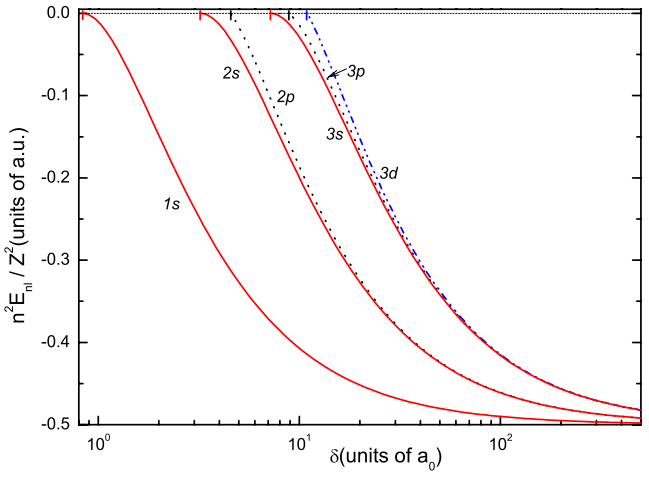

FIG. 1. (Color online) Scaled energies of $1s$, $2l$, $3l$ bound states as a function of scaled screening length δ.

$$V_{eff} = \frac{l(l+1)}{2\rho^2} - \frac{1}{\rho}\exp(-\rho/\delta), \tag{13}$$

which under certain conditions supports quasibound states (resonances). The quasibound states in the potential [Eq. (13)] have been subject to numerous studies in the past ([32–34], and references therein) and the conditions for their appearance have been firmly established. In Ref. [34] it was shown that bound states and resonances in the potential [Eq. (13)] exist for $l(l+1)/(2\delta) < 0.367\,879$, while for $0.367\,879 \leq l(l+1)/(2\delta) < 0.419\,981$ the potential supports only quasibound states. For $l(l+1)/(2\delta) \geq 0.419\,981$ the potential [Eq. (13)] supports neither bound nor quasibound state. These relations are derived from the mutual positions of the minimum of the "inner" well of the potential [Eq. (13)] and the maximum of its centrifugal barrier. For $l(l+1)/(2\delta) = 0.419\,981$ these two extrema of the potential merge into one another.

The existence of quasibound states in the effective potential of Eq. (2) for $l > 0$ has obvious consequences for the near-threshold photoionization: the continuum electron with $l > 0$ can be temporarily trapped in these states and the overlap of its wave function with the initial bound-state wave function can be very large. Therefore, when the screening length δ becomes smaller than δ^c_{nl} $(l > 0)$, i.e., when a given nl state (energetically lying above the initial state) enters the region of its quasibound states, the photoionization cross section will exhibit strong enhancement (resonances) at photoelectron energies below the maximum of the centrifugal barrier, i.e., for $\varepsilon \leq 0.037\,870/\delta$ [33]. The cross section enhancement will be most pronounced for the lowest quasibound state for which the centrifugal potential barrier presents the largest width, i.e., the one lying closest to δ^c_{nl}. We should note that for a given l-continuum wave there exist many critical screening lengths δ^c_{nl} belonging to different n (see Table I) below which (i.e., for $\delta \leq \delta^c_{nl}$) the bound nl state becomes quasibound. Each of these series of resonances can appear in the cross section at energies inversely proportional to δ^c_{nl}. As mentioned above, the series of quasibound states associated with a given δ^c_{nl} terminates at $\delta_0(l) = [l(l+1)/2]/0.419\,981$. We should note that when passing through a resonance at a given energy ε_r, the phase shift Δ_l of the continuum electron wave function changes by π radians [17,36] (see also Sec. II B 3).

For the continuum s-wave functions the effective potential does not exhibit any barrier. Nevertheless, as it is well known from the low-energy elastic particle scattering on short-range potentials [17,36], the s-wave function can be significantly enhanced in the interior region of the potential $(\rho \leq \delta)$ for values of the screening parameter for which the scattering length a_s becomes large. This later happens when the potential supports a bound or virtual (positive energy) state with near-zero energy. The momenta κ of these states are close to the inverse values of the scattering length $(\kappa \approx 1/a_s)$ and when $a_s > 0$ the state is bound, while when $a_s < 0$ the state is virtual [17,36]. This follows from the

TABLE I. Values of the critical scaled screening lengths, $\delta_{nl} = ZD_{nl}(a_0)$.

	l					
n	0	1	2	3	4	5
1	0.839907 (0.839908)[a]					
2	3.222559 (3.223)	4.540956 (4.541)				
3	7.171737 (7.171)	8.872221 (8.872)	10.947492 (10.947)			
4	12.686441 (12.687)	14.730720 (14.731)	17.210209 (17.210)	20.067784 (20.068)		
5	19.770154 (19.772)	22.130652 (22.130)	24.984803 (24.985)	28.257063 (28.257)	31.904492 (31.904)	
6	28.427266 (28.423)	31.080167 (31.079)	34.285790 (34.285)	37.949735 (37.950)	42.018401 (42.018)	46.458584 (46.458)

[a]Reference [30].

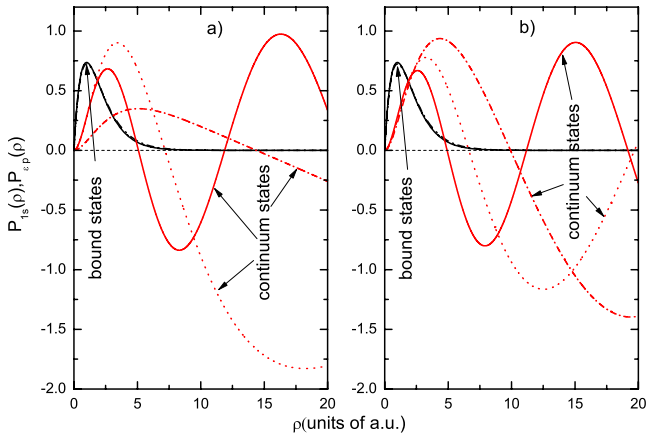

FIG. 2. (Color online) Ground state wave function P_{1s} and continuum wave function $P_{\varepsilon p}$ as function of ρ for the unscreened case and the screened cases with $\delta=9a_0$ and $\delta=5a_0$. Panel (a): $\varepsilon=0.001$ Ry; panel (b): $\varepsilon=0.03$ Ry. Solid lines: unscreened case; dotted lines: $\delta=9a_0$; and dashed-dotted lines: $\delta=5a_0$. The bound-state wave functions are in black.

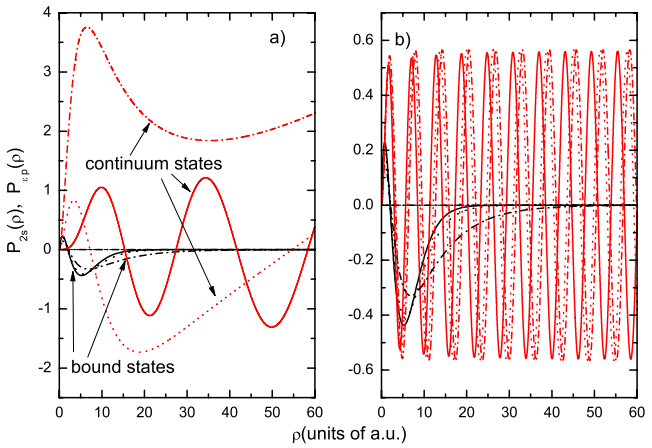

FIG. 3. (Color online) Bound-state wave function P_{2s} and continuum wave function $P_{\varepsilon p}$ as a function of ρ for the unscreened case and the screened cases with $\delta=9a_0$ and $\delta=4.5a_0$. Panel (a): $\varepsilon=0.0003$ Ry; panel (b): $\varepsilon=1.0$ Ry. Solid lines: unscreened case; dotted lines: $\delta=9a_0$; and dashed-dotted lines: $\delta=4.5a_0$. The bound-state wave functions are in black.

effective-range theory expansion of the s-wave phase shift [17,36]

$$k\cot\Delta_s(k) = -\frac{1}{a_s} + O(k^2), \tag{14}$$

which for $k\to 0$ defines the poles of the scattering matrix in the complex plane of the momentum k (lying, in this case, on the imaginary axis). We should keep in mind that $\Delta_s(k)$ (and hence a_s) depends also on δ.

The present calculations have shown (see Sec. II B 3) that the near-zero-energy s states in Debye-Hückel potential appear when $\delta \leq \delta_{ns}^c$ $(n>1)$. When the energy of continuum s-wave function is close to the energy of these states its phase shift changes by π radians.

2. Behavior of bound and continuum wave functions

The overlap of the initial and final state wave functions in the photoionization transition $nl\to\varepsilon l'$ to a large extent determines the magnitude of the cross section. Therefore, most of the differences between the photoionization cross section in the Coulomb and Debye-Hückel potentials can be observed already on the level of differences in the bound-state and continuum wave functions. Generally, the bound-state wave functions in the screened case have smaller peaks (positive or negative) than in the unscreened case, but shifted toward higher ρ, and the wave function values in the asymptotic region are larger than those in the unscreened case [30,35]. These properties become more expressed as the screening length decreases. As we shall see below, the continuum electron wave functions in the screened case are "pushed out" further from the coordinate origin than in the pure Coulomb case, their amplitudes increase, and frequency decreases with decreasing δ. These properties become more expressed at smaller photoelectron energies.

In Figs. 2–5 we show the scaled bound-state wave functions $P_{nl}(\rho)$ of the $1s,2s,2p$ states and the scaled continuum wave functions $P_{\varepsilon l}(\rho)$ for $l=0,1,2$ partial waves for the pure Coulomb and Debye-Hückel potentials with a number of screening lengths δ. In Fig. 2 we show the wave functions $P_{1s}(\rho)$ and $P_{\varepsilon p}(\rho)$ for the unscreened case and the screened case with $\delta=9a_0$ and $\delta=5a_0$ for photoelectron energies of 0.001 Ry [panel (a)] and 0.03 Ry [panel (b)]. In both panels we see that the bound-state $P_{1s}(\rho)$ wave functions for these two screening lengths are very close to that of the unscreened case. However, both panels also show that the continuum wave functions $P_{\varepsilon p}(\rho)$ for $\delta=9a_0$ and $\delta=5a_0$ differ substantially from that of the unscreened case both in amplitude and in phase. The $P_{\varepsilon p}(\rho)$ wave function for $\delta=9a_0$ in Fig. 2(a) for the photoelectron energy $\varepsilon=0.001$ Ry in the region of ρ close to the coordinate origin has the same gradient as the wave function of the unscreened case, but after the latter attains its first maximum the screened case wave function continues to increase and attains its maximum at a much larger value of ρ. It is obvious from the figure that the over-

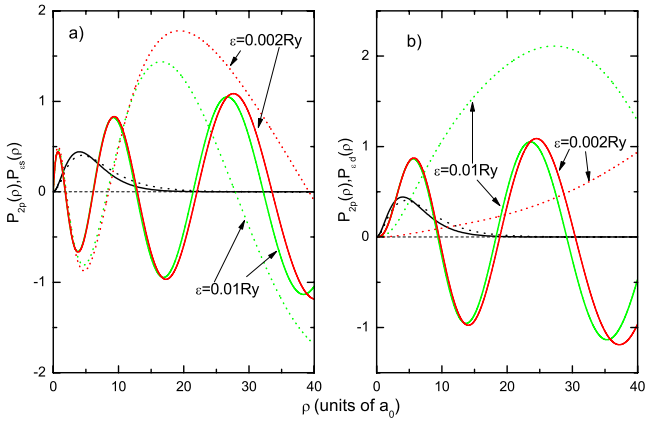

FIG. 4. (Color online) Bound-state wave function P_{2p} and the continuum wave functions $P_{\varepsilon s}$ [panel (a)] and $P_{\varepsilon d}$ [panel (b)] as a function of ρ for the pure Coulomb case and for the screened case with $\delta=8a_0$. Solid lines: unscreened case; dotted lines: $\delta=8a_0$. The bound-state wave functions are in black.

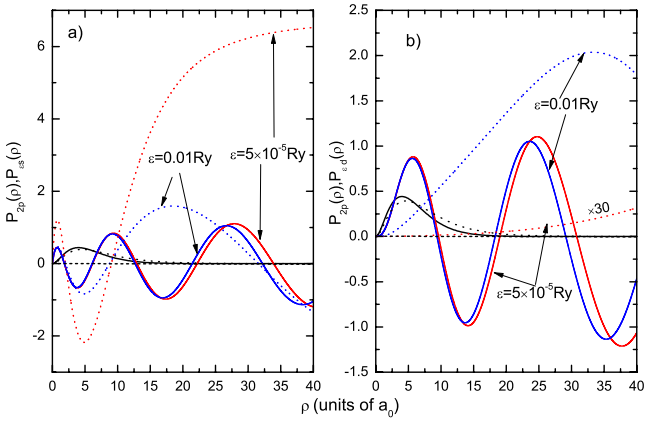

FIG. 5. (Color online) Bound-state wave function P_{2p} and continuum functions $P_{\varepsilon s}$ [panel (a)] and $P_{\varepsilon d}$ [panel (b)] as a function of ρ for the pure Coulomb case (solid lines) and the screening case with $\delta=7.1a_0$ (dotted lines). The black lines are for the bound states. The d-wave function for $\varepsilon=5\times10^{-5}$ Ry is multiplied by 30 times in order to be visible.

lap of $P_{\varepsilon p}(\rho)$ and $P_{1s}(\rho)$ wave functions in the screened case with $\delta=9a_0$ at the considered energy is larger than in the unscreened case and, consequently, the corresponding photoionization cross section for this energy is larger than in the unscreened case. For the Debye screening length $\delta=5a_0$ the $P_{\varepsilon p}(\rho)$ continuum wave function has much smaller gradient than that for the unscreened case, its first maximum is smaller and pushed out to a larger value of ρ, so that the overlap of $P_{\varepsilon p}(\rho)$ and $P_{\varepsilon l}(\rho)$ wave functions in the screened case with $\delta=5a_0$ is smaller than that in the unscreened case resulting in a smaller photoionization cross section for this energy. In Fig. 2(b), the photoelectron energy is higher, $\varepsilon=0.03$ Ry, the $P_{\varepsilon p}(\rho)$ wave functions for both $\delta=9a_0$ and $\delta=5a_0$ have gradients in the region near the coordinate origin as the $P_{\varepsilon p}(\rho)$ wave function of the unscreened case but their first maxima are significantly larger than that of the Coulomb wave function and are located at larger values of ρ (as are their first nodes). Their overlap with the corresponding bound-state wave functions is obviously significantly larger than that in the unscreened case, and so are the corresponding cross sections for this energy. It should be noted, however, that although the first maximum and the first node of the $P_{\varepsilon p}(\rho)$ wave function in the $\delta=5a_0$ screening case are significantly larger than in the $\delta=9a_0$ screened case, that does not affect significantly their overlap with the corresponding bound-state wave functions and, consequently, the photoionization cross sections for $\delta=9a_0$ and $\delta=5a_0$ will be close for this photoelectron energy. Both panels of Fig. 2 show that the continuum wave functions are much more sensitive to the variation of the screening length than the bound-state wave functions.

In Fig. 3 we show the wave functions $P_{2s}(\rho)$ and $P_{\varepsilon p}(\rho)$ for the screening lengths $\delta=9a_0$ and $\delta=4.5a_0$ for the photoelectron energies of $\varepsilon=0.0003$ Ry [panel (a)] and $\varepsilon=1$ Ry [panel (b)]. It can be remarked on these figures that while for $\delta=9a_0$ the bound-state wave function is close that of the unscreened case, the $P_{2s}(\rho)$ wave function for the screened case with $\delta=4.5a_0$ differs from that of the pure Coulomb case in reduced peak values, their shift to larger ρ, and in its larger radial extension. The $P_{\varepsilon p}(\rho)$ continuum wave function for $\delta=9a_0$ in Fig. 3(a) has basically similar behavior as that in Fig. 2(a) except that its oscillation period is much larger (due to the much smaller photoelectron energy). However, the $P_{\varepsilon p}(\rho)$ wave function for $\delta=4.5a_0$ in Fig. 3(a) has a drastically different behavior than that of $P_{\varepsilon p}(\rho)$ in Fig. 2(a) despite the fact that the screening length $\delta=4.5a_0$ is not much different than $\delta=5a_0$. The different character of the behavior of $P_{\varepsilon p}(\rho)$ wave function for $\delta=4.5a_0$ in Fig. 3(a) cannot be ascribed to the much lower photoelectron energy in this case but rather to the fact that the screening length $\delta=4.5a_0$ is slightly below the critical screening length $\delta^c_{2p}=4.541a_0$ at which the $2p$ bound state enters the continuum (see Table I). Hence, the $P_{\varepsilon p}(\rho)$ wave function for $\delta=4.5a_0$ in Fig. 3(a) shows the behavior of a continuum wave function when trapped by a quasibound state of the potential. The large positive amplitude of this continuum wave function, extending to distances from the coordinate origin much larger than the effective extension of the $P_{2s}(\rho)$ wave function, ensures a strongly enhanced photoionization cross section at appropriate photoelectron energies (resonance).

In Fig. 3(b) the $P_{2s}(\rho)$ and $P_{\varepsilon p}(\rho)$ wave functions for the same screening lengths are shown but for an energy of continuum electron of 1 Ry. The strong oscillations of the continuum wave functions at this energy make the photoionization cross section small. The cross section is determined only by the behavior of the wave function at radial distances close to the coordinate origin. In this region, as Fig. 3(b) shows, the continuum wave functions in the screened case are very close to that of the unscreened case, while the bound-state wave functions have amplitudes smaller than that of the unscreened case. Therefore, the photoionization cross section in the screened case will be smaller than that in the pure Coulomb case. This conclusion obviously holds also for energies larger than 1 Ry.

In Fig. 4 the bound-state wave function $P_{2p}(\rho)$ and continuum wave functions $P_{\varepsilon s}(\rho)$ and $P_{\varepsilon d}(\rho)$ (at photoelectron energies $\varepsilon=0.01$ Ry and $\varepsilon=0.002$ Ry) are shown in the unscreened case and in the screened case with $\delta=8a_0$. It is important to observe that in the unscreened case the wave functions $P_{\varepsilon s}(\rho)$ and $P_{\varepsilon d}(\rho)$ for these two energies start to differ from each other only in the region of ρ where their overlap with the bound-state wave function $P_{2p}(\rho)$ becomes negligibly small. In the screened case, however, the diffuse character of the $P_{\varepsilon d}(\rho)$ wave function is clearly pronounced, especially when the photoelectron energy decreases. In Fig. 4(a) we see that the $P_{\varepsilon s}(\rho)$ wave functions for the two energies in the screened case start to differ from each other only after reaching their second extremum, i.e., in the region of ρ where their overlap with the $P_{2p}(\rho)$ wave function is small. Thus, the cross section for the $2p\rightarrow\varepsilon s$ transition will attain its maximum value already at energies of about $\varepsilon=0.002$ Ry (and perhaps even below). In contrast to this, the diffuse character of the $P_{\varepsilon d}(\rho)$ wave function [see Fig. 4(b)] makes its overlap with the $P_{2p}(\rho)$ wave function at the energy of $\varepsilon=0.002$ Ry very small (and more so for still lower energies). As Fig. 4(b) indicates (the curve for $\varepsilon=0.01$ Ry), the overlap of $P_{2p}(\rho)$ and $P_{\varepsilon d}(\rho)$ wave functions increases with increasing the energy of ejected electron, and for the

screening length $\delta=8a_0$ it will maximize at energies larger than $\varepsilon=0.01$ Ry. This will also be reflected in the cross section for the $2p\rightarrow\varepsilon d$ transition. The displacement of the maxima of the cross sections for $2p\rightarrow\varepsilon s$ and $2p\rightarrow\varepsilon d$ transitions on the photoelectron energy scale will result in a minimum in the photoionization cross section of the $2p$ state (Combet-Farnoux minimum). However, since at higher energies the matrix element for the $2p\rightarrow\varepsilon d$ transition is usually much larger than that for the $2p\rightarrow\varepsilon s$ transition, the Combet-Farnoux minimum is not so strongly pronounced if visible at all.

In Fig. 5 we show the radial dependences of $P_{2p}(\rho)$, $P_{\varepsilon s}(\rho)$ [panel (a)] and $P_{2p}(\rho)$, $P_{\varepsilon d}(\rho)$ [panel (b)] wave functions in the unscreened and the screened cases with $\delta=7.1a_0$ for photoelectron energies of 0.01 and 5×10^{-5} Ry. As in the case of Fig. 4, the $P_{2p}(\rho)$ wave functions in the screened and unscreened cases do not differ much one from another, neither do so the continuum wave functions in the unscreened case for the two very different energies (except for the phase shift increase with decreasing the energy). One can see from Figs. 5(a) and 5(b) that at the energy of 0.01 Ry the screened $P_{\varepsilon s}(\rho)$ continuum wave function has much bigger overlap with the $P_{2p}(\rho)$ wave function for small values of ρ than the $P_{\varepsilon d}(\rho)$ wave function which can lead to a Combet-Farnoux minimum in the total photoionization cross section at energies close to 0.01 Ry. The most remarkable feature in this figure is, however, the drastic difference in the behavior of the $P_{\varepsilon s}(\rho)$ and $P_{\varepsilon d}(\rho)$ screened wave functions for the photoelectron energy of 5×10^{-5} Ry. While the magnitude of $P_{\varepsilon d}(\rho)$ wave function in the range of radial distances up to $40a_0$ is extremely small, the screened $P_{\varepsilon s}(\rho)$ wave function after its first oscillating period shows a dramatic increase of its amplitude with increasing ρ. We should note that the screening length $\delta=7.1a_0$ for this function is slightly below the critical screening length of the $3s$ state ($\delta^c_{3s}=7.171a_0$; see Table I), i.e., it is in the region where potential virtual states can be found provided the energy is small enough. Apparently, the energy of 5×10^{-5} Ry is still relatively far (larger) from the energy of the virtual s state since the wave function in Fig. 5(a) for this energy does not show the typical behavior of a virtual-state wave function that should continuously increase from the origin [17,36]. Nevertheless, the large amplitudes of $P_{\varepsilon s}(\rho)$ over the entire region of radial extension of bound-state wave function ensure a significant enhancement of the $2p\rightarrow\varepsilon s$ photoionization cross section. [As we shall see in Fig. 9(b), the maximum of this enhancement occurs at $\sim1\times10^{-5}$ Ry for the same value of the screening length, $\delta=7.1a_0$.]

3. Behavior of the phase shifts

As evident from Figs. 2–5, the phase shifts of the continuum wave functions exhibit significant changes when the Coulomb potential is screened. The variations of the phase shifts with the screening length for the s-, p-, and d-continuum waves are shown in Fig. 6 for photoelectron energies of 1.0×10^{-4} Ry [panel (a)] and 1.0×10^{-3} Ry [panel (b)] and are expressed in mod π. The figures show that for a given energy the phase shifts increase with increasing δ. They also show that when δ approaches certain critical values, the phase shift passes through $\pi/2$ (mod π). The region of δ in which the phase changes for π radians is narrower for the smaller critical screening lengths than for the larger ones, this property being much more pronounced for the smaller photoelectron energy.

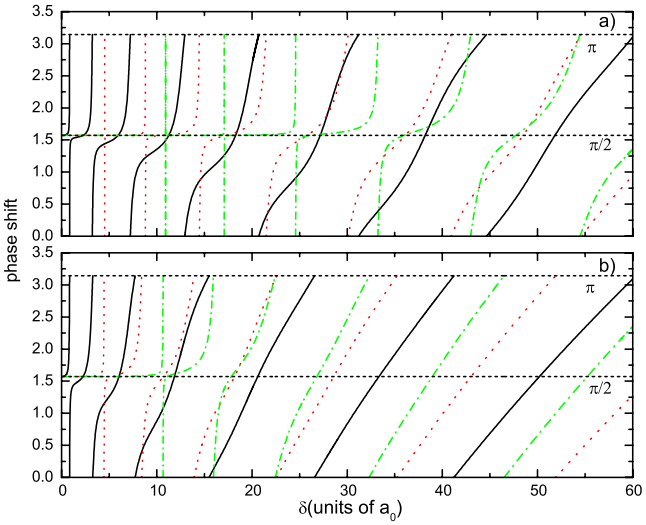

FIG. 6. (Color online) Phase shifts of the continuum s-, p-, and d-wave functions as a function of screening length δ. Panel (a): $\varepsilon=0.0001$ Ry; panel (b): $\varepsilon=0.001$ Ry. Black solid line: s wave; red dotted line: p-wave; and green dashed-dotted line: d wave.

It should be noted in these figures that the critical screening lengths at which the s-wave phase shift passes through $\pi/2$ (mod π) coincide with the critical screening lengths δ^c_{ns} (see Table I). Similarly, the critical screening lengths at which the p-wave and d-wave phase shifts pass through $\pi/2$ (mod π) coincide with the critical screening lengths δ^c_{np} and δ^c_{nd}, respectively (see Table I). As we have discussed in Sec. II B 1 above, the regions $\delta\sim\delta^c_{ns}$ and $\delta\leq\delta^c_{nl}$ ($l>0$) are related to the near-zero-energy s states and the quasibound $l>0$ states, respectively, responsible for the cross section enhancement features. It should also be noted in Fig. 6 that with increasing δ the region around δ^c_{nl} in which the phase shift changes for π radians becomes increasingly broader (especially for higher energies) which can be related to the gradual disappearance of mentioned photoionization cross section enhancement features (i.e., approach to the pure Coulomb case).

In Fig. 7 we show the energy dependence of the s-wave and p-wave phase shifts near the critical screening lengths $\delta^c_{2s}=3.223\,635a_0$ [panel (a)] and $\delta^c_{3p}=8.872\,221a_0$ [panel (b)], respectively, for a number of near-lying δ values. The figures show that the energy behavior of Δ_s and Δ_p phase shifts near the corresponding critical screening lengths is quite different. With decreasing the photoelectron energy, the Δ_s phase shift for $\delta<\delta^c_{2s}$ increases from its high-energy value π toward $3\pi/2$ and after certain energy it starts again to decrease toward its zero-energy value π. For $\delta>\delta^c_{2s}$ the Δ_s phase shift passes though the value $3\pi/2$ and with decreasing the energy tends to its zero-energy value of 2π. Only for $\delta=\delta^c_{2s}$ the Δ_s phase shift when reaching the value of $3\pi/2$ during the decrease of the energy maintains this value down to the zero-energy limit. According to Eq. (14), the

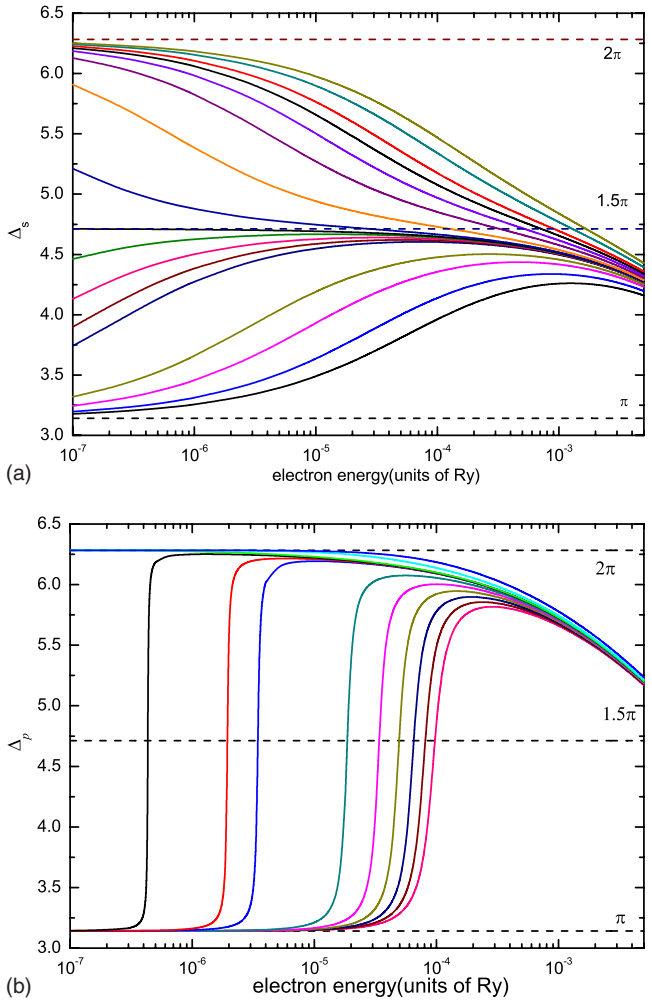

FIG. 7. (Color online) Energy behavior of s-wave [panel (a)] and p-wave [panel (b)] phase shifts near the critical Debye lengths δ_{2s}^c and δ_{3p}^c, respectively. The lines in panel (a) are for δ=3.160a_0, 3.180a_0, 3.200a_0, 3.210a_0, 3.220a_0, 3.221a_0, 3.222a_0, 3.223a_0, 3.223 635a_0, 3.225$a_0$3.230a_0, 3.240a_0, 3.250a_0, 3.260a_0, 3.270a_0, 3.290a_0, 3.310a_0 counted from bottom to top successively and those in panel (b) are for δ=8.810a_0, 8.820a_0, 8.830a_0, 8.840a_0, 8.850a_0, 8.860a_0, 8.870a_0, 8.871a_0, 8.872a_0, 8.872 221a_0, 8.890a_0, 8.930a_0 counted from bottom to top.

scattering length for this value of the phase shift becomes infinite (i.e., the virtual or bound s state for $\delta=\delta_{2s}^c$ has a zero binding energy) and the photoionization cross section will diverge at the threshold (as $1/\varepsilon$) [17,36].

From the discussion in Sec. II B 1 we know that for $\delta<\delta_{2s}^c$ there is only one bound s state in the atom (namely, the 1s state), while for $\delta_{3s}^c>\delta>\delta_{2s}^c$ there are two such states (1s and 2s). Figure 6(a), thus, demonstrates the validity of Levinson's theorem [17,36] for the Debye-Hückel potential.

The phase shift Δ_p [Fig. 7(b)] for a given $\delta\leq\delta_{3p}^c$ exhibits at very low photoelectron energies (below $\sim 10^{-6}$ Ry) a sharp jump from π to 2π radians and then slowly decreases when the energy increases. When the difference $\delta_{3p}^c-\delta$ increases the jump of the phase shift takes place at higher energies; it becomes less sharp and does not reach the value of 2π but rather the envelop defined by the phase shift for $\delta=\delta_{3p}^c$. As discussed earlier, in the region $\delta\leq\delta_{3p}^c$ there are quasibound states generated by the exit of 3p bound state into the continuum and the observed Δ_p energy behavior in Fig. 7(b) is typical for the scattering on such states. For $\delta>\delta_{3p}^c$ the Δ_p phase shifts continue to increase with increasing δ and all tend to their zero-energy limit 2π when the energy decreases. We see from Fig. 7(b) that the Δ_p phase shifts for all $\delta<\delta_{3p}^c$ have a zero-energy value of π radians, consistent with the Levinson theorem (the only bound p state in this region of δ is the 2p state).

The behavior of s- and p-wave phase shifts near any of the critical screening lengths δ_{ns}^c and δ_{np}^c, respectively, is similar to that shown in Figs. 7(a) and 7(b).

III. PHOTOIONIZATION CROSS SECTIONS

A. Scaled cross sections

The total photoionization cross section of a hydrogenlike ion with nuclear charge Z in the nl state in the nonrelativistic approximation is given by [28]

$$\sigma_{nl}=\frac{8\pi^2\alpha a_0^2}{3(2l+1)}\Delta E[lR_{l-1}^2(Z,D)+(l+1)R_{l+1}^2(Z,D)], \quad (15)$$

where α is the fine-structure constant, a_0 is the Bohr radius, ΔE is the difference energy between the bound and continuum states, and $R_{l\pm1}(Z,D)$ are the radial matrix elements for the $nl\rightarrow E$, $l\pm1$ dipole transition given by (in the length form)

$$R_{l\pm1}(Z,D)=\langle P_{nl}(r;Z,D)|r|P_{El\pm1}(r;Z,D)\rangle. \quad (16)$$

Here r is the electron radial position, E is the continuum electron energy, and $P_{nl}(r;Z,D)$ and $P_{E,l\pm1}(r;Z,D)$ are the bound and continuum electron radial wave functions, respectively.

Using the scaling transformation [Eq. (3)] and the scaled continuum wave function [Eq. (12)], we obtain the dipole matrix element for the bound-free $nl\rightarrow El\pm1$ transition in the total photoionization cross section in scaled form,

$$\begin{aligned}R_{l\pm1}(Z,D)&=\langle P_{nl}(r;Z,D)|r|P_{El\pm1}(r;Z,D)\rangle\\&=Z^{-2}\langle P_{nl}(\rho;\delta)|\rho|P_{\varepsilon l'}(\rho;\delta)\rangle=Z^{-2}R_{l\pm1}(\delta),\end{aligned} \quad (17)$$

$$\sigma_{nl}(E,Z,D)=Z^{-2}\sigma_{nl}(\varepsilon,\delta). \quad (18)$$

As a basic check of the numerical accuracy of photoionization cross section calculations serve the f-sum rule [28],

$$\sum_{l'}\left(\sum_{n'}f_{nl,n'l'}+\int_0^\infty dk f_{nl,kl'}\right)=1, \quad (19)$$

where $f_{nl,n'l'}$ and $f_{nl,kl'}$ are the usual oscillator strength and oscillator strength density, respectively. The oscillator strengths for the bound-bound transitions have been calculated in our previous work [25] using the same symplectic integration scheme. In Table II we give the f-sum values for the Lyman series for the unscreened case and for the screened one for a number of screening lengths. The departure from one appears at the fourth digit.

TABLE II. Oscillator strengths and f-sum rule of the Lyman series for a number of scaled screening Debye lengths $\delta(a_0)$.

	δ						
$1s-np$	∞	50	20	11	9	5	1
2	0.4162	0.4137	0.4018	0.3718	0.3511	0.1933	
3	0.0791	0.0766	0.0659	0.0385	0.0156		
4	0.0290	0.0261	0.0145				
5	0.0139	0.0107					
6	0.0078	0.0044					
7	0.0048	0.0014					
Discrete spectrum	0.5650	0.5329	0.4822	0.4103	0.3667	0.1933	
Continuous spectrum	0.4357	0.4668	0.5176	0.5894	0.6330	0.8065	1.0001
Total	1.0007	0.9997	0.9999	0.9997	0.9997	0.9998	1.0001

In Secs. III B and III C we shall present the results of our photoionization cross section calculations for the initial $1s$, $2l$, $3l$ states for a number of screening lengths and for the unscreened case for comparison purposes. The calculations have been performed in the photoelectron energy range from 10^{-6} to 20 Ry. The selection of screening lengths in each of these calculations has been made so as to illustrate one or more of the characteristic features of photoionization cross section when the electron-ion interaction is screened. We shall group our calculated cross sections into two groups: those for which the initial state wave function has nodes and those for which it does not. The numerous photoionization cross section calculations for many-electron isolated atoms (or ions) [14,20–22,37–40] have shown that the Cooper minima appear only when the initial state wave function has at least one node. When the atom (ion) is in its ground state (the case for which most of the calculations have been performed) the additional condition for their appearance is that $nl \rightarrow \varepsilon l'$ transition is of the $l \rightarrow l+1$ type.

B. Initial state wave functions without nodes ($n-l-1=0$)

In our set of calculations the wave functions of $1s, 2p, 3d$ initial states have no nodes. Their total and l'-channel ($l \rightarrow l'=l\pm 1$) cross sections are displayed in Figs. 8–10 for the screened case with a number of screening lengths and for the pure Coulomb case.

In Fig. 8 the $1s \rightarrow \varepsilon p$ photoionization crosses section [panel (a)] and the corresponding matrix element [panel (b)] for the unscreened and screened cases with Debye lengths $\delta=50a_0, 20a_0, 9a_0, 8.86a_0, 5a_0, 4.52a_0, 1a_0$. Figure 8(a) shows that, unlike the cross section in the pure Coulomb case which has a constant zero-energy value [28] [maintained in Fig. 8(a) up to photoenergies as high as $\sim 10^{-2}$ Ry], the cross sections with screened Coulomb interaction obey the Wigner threshold law $k^{2l'+1}=k^3=(2\varepsilon)^{3/2}$ as expected. The energy at which the Wigner threshold law starts to determine the low-energy cross section behavior depends on the value of the screening length δ and generally decreases with increasing δ. After leaving the threshold energy region, the cross sections of the screened cases become larger than the cross section of the pure Coulomb case, but in the asymptotic energy region (above a few rydbergs) they are slightly smaller than that of the Coulomb case. As we have discussed in Sec. II B 2 [see Fig. 3(b)], at these energies the continuum wave function penetrates deeply in the inner part of the potential which has dominantly Coulomb character. On the other hand, for very small screening lengths the maximum of the $1s$ wave function is substantially reduced which leads to reduction of the cross section as well [as exemplified with the cross section for $\delta=1a_0$ in Fig. 7(a)].

Perhaps the most remarkable features in Fig. 8(a) are the two resonances at $\varepsilon \sim 2.58\times 10^{-4}$ Ry and $\varepsilon \sim 1.85 \times 10^{-5}$ Ry for the screening lengths $\delta=4.52a_0$ and $\delta=8.86a_0$, respectively, whose peaks are about three orders of magnitude larger than the cross section values of other screened cases considered. The first of these δ values lies in the region of quasibound states associated with the critical screening length of the $2p$ bound state [$\delta^c_{2p}=4.541a_0$ (see Table I)], while the second one is associated with the quasi-

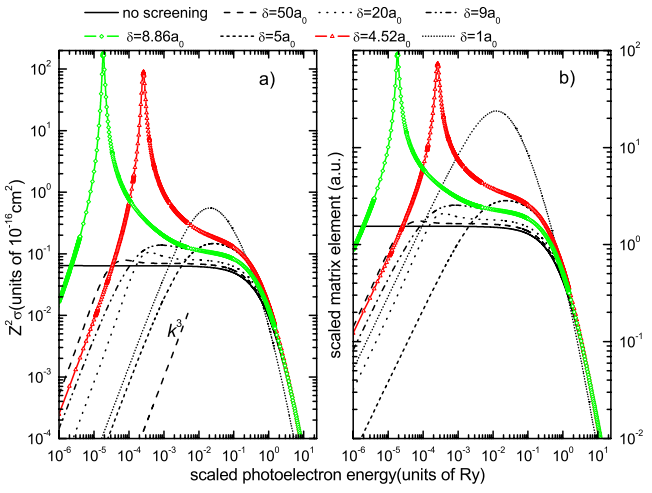

FIG. 8. (Color online) (a) Scaled photoionization cross sections for the ground state $1s$ as a function of scaled photoelectron energy for the pure Coulomb case and for the screened case with scaled screening lengths $\delta=50a_0, 20a_0, 9a_0, 8.86a_0, 5a_0, 4.52a_0, 1a_0$. Panel (b): dipole matrix elements.

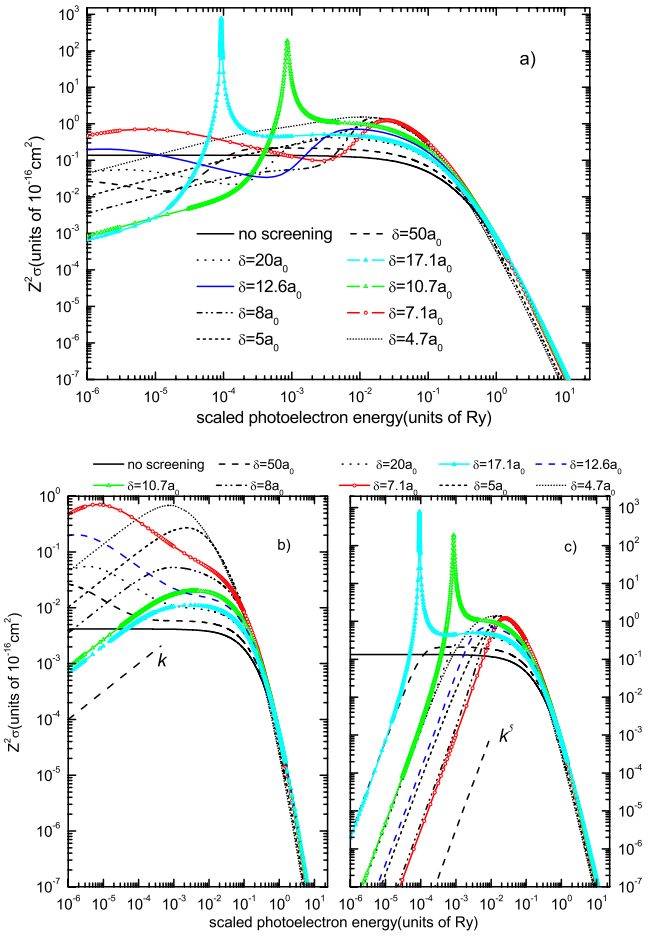

FIG. 9. (Color online) Scaled photoionization cross sections for the $2p$ state as a function of the scaled photoelectron energy for the pure Coulomb case and for the screened case with scaled screening lengths $\delta=50a_0, 20a_0, 11a_0, 8a_0, 5a_0, 4.7a_0$. Panel (a): total cross sections; panels (b) and (c): cross sections for the $2p\rightarrow\varepsilon s$ and $2p\rightarrow\varepsilon d$ channels, respectively.

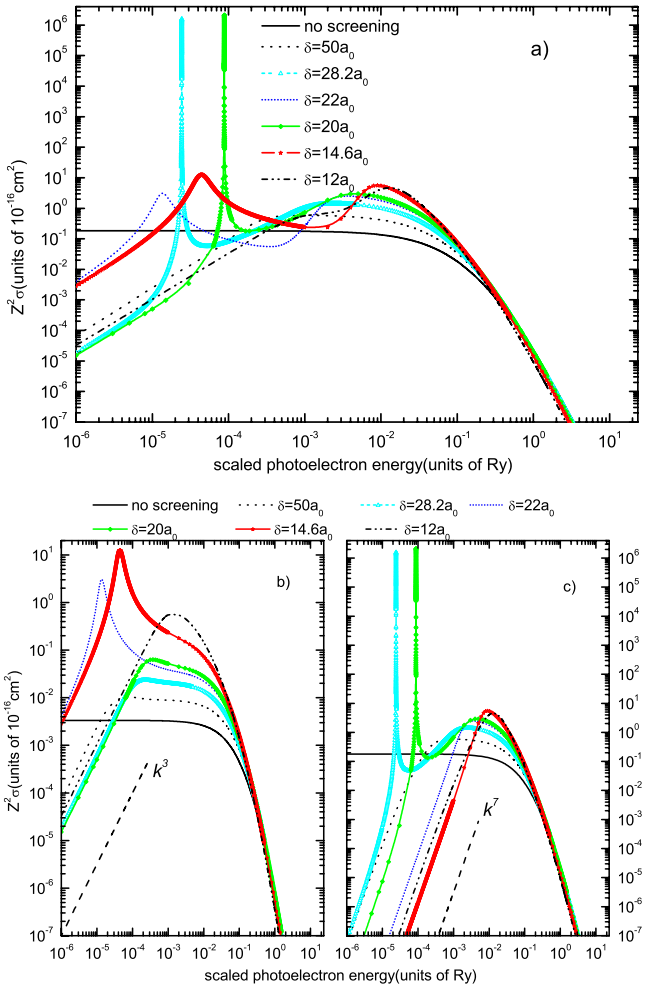

FIG. 10. (Color online) Scaled photoionization cross sections for the $3d$ state as a function of the scaled photoelectron energy for the pure Coulomb case and the scaled screening lengths $\delta=50a_0, 28.2a_0, 22a_0, 20a_0, 14.6a_0, 12a_0$. Panel (a): total cross sections; panels (b) and (c): cross sections for the $3d\rightarrow\varepsilon p$ and $3d\rightarrow\varepsilon f$ channels, respectively.

bound states in the region $\delta\leq\delta^c_{3p}(=8.872a_0)$. Obviously, in accordance with our discussion in Sec. II B 1, for any value of δ in the region $\delta_0(l=1)<\delta\leq\delta^c_{np}$ $[n>2,\ \delta_0(l=1)=2.381\,06a_0$ (see Sec. II B 1)] there will be a resonance in the photoionization cross section the peak values of which will rapidly decrease with the increase of the difference $\delta^c_{np}-\delta$. As Fig. 8(a) demonstrates, the energies at which these resonance series appear are inversely proportional to the value of δ^c_{np} (see also Sec. II B 1).

We should note that energy behavior of the cross section in Fig. 8(a) mimics the energy behavior of the matrix elements shown in Fig. 8(b). This is the case with all photoionization $nl\rightarrow\varepsilon l'$ cross sections for which the initial bound-state wave function does not have nodes.

In Table III we compare our $1s\rightarrow\varepsilon p$ photoionization cross sections with those in Ref. [8] for $\delta=5a_0$ and $\delta=20a_0$ for a number of photon energies between 0.33 and 10 a.u. We observe a very good agreement between the two sets of calculations.

In Fig. 9 we show the total photoionization of $2p$ state [panel (a)] and the cross sections for the $2p\rightarrow\varepsilon s$ [panel (b)] and $2p\rightarrow\varepsilon d$ [panel (c)] photoionization channels. The selected screening lengths in this case are $\delta=50a_0, 20a_0, 17.1a_0, 12.6a_0, 10.7a_0, 8.0a_0, 7.1a_0, 5a_0, 4.7a_0$. The total photoionization cross section in Fig. 9(a) is just a

TABLE III. Photoionization cross sections for H($1s$) (in units of 10^{-16} cm^2) for two Debye screening lengths δ and a number of photon energies ω. The numbers in parentheses are powers of 10.

ω	$\delta=5a_0$ ($\varepsilon_{1s}=0.3268$ a.u.)		$\delta=20a_0$ ($\varepsilon_{1s}=0.4518$ a.u.)	
(a.u.)	Present	Ref. [8]	Present	Ref. [8]
0.338	0.14603	0.14594		
0.34	0.14674	0.14665		
0.453	0.07272	0.07268	0.08233	0.08227
0.455	0.0719	0.07186	0.08022	0.08017
1	0.00861	0.0086	0.00926	0.00926
10	7.78001(−6)	7.77958(−6)	8.18091(−6)	8.1638(−6)

sum of $2p \rightarrow \varepsilon s$ and $2p \rightarrow \varepsilon d$ channel cross sections which we shall briefly analyze now.

The $2p \rightarrow \varepsilon s$ channel cross sections [Fig. 9(b)] for all selected screening lengths in a broad energy region around their maxima are significantly larger than the cross section in the unscreened case, with peak values of about one to two orders larger than the Coulomb cross section. The cross sections for the screening lengths $\delta = 50a_0, 20a_0, 12.6a_0, 7.1a_0$ exhibit broad resonances at photoelectron energies below $\sim 10^{-4}$ Ry, while those for the other values of the screening length start to obey the Wigner threshold law ($k^{2l'+1} = k$) already at energies a few times 10^{-4} Ry. The appearance of broad low-energy resonances in the $2p \rightarrow \varepsilon s$ channel cross sections for the above listed values of δ is due to the fact that all these are close to the zero-energy values of the bound $3s$, $4s$, $5s$, and $8s$ states whose critical screening lengths are $\delta^c_{3s} = 7.171a_0$, $\delta^c_{4s} = 12.687a_0$, $\delta^c_{5s} = 19.772a_0$ (see Table I), and $\delta^c_{8s} = 50.44a_0$ (see [30]). Except for the $\delta = 20a_0$ case where this value is slightly larger than δ^c_{5s}, in all other cases the selected screening length is slightly smaller than the corresponding δ^c_{ns}. As discussed in Sec. II B 1, these near-zero-energy (virtual) states are the cause for the observed broad resonances in the near-threshold energy region of $np \rightarrow \varepsilon s$ cross section, as further evidenced by the change of the s-wave phase shift by π radians when δ passes the values δ^c_{ns} observed in Fig. 5. At energies well below the broad resonance, the photoionization cross section will, of course, again follow the Wigner threshold law.

It is interesting to observe in Fig. 9(b) that the cross sections for $\delta = 5a_0$ and $\delta = 4.7a_0$ have maxima in the energy range of 10^{-3}–10^{-2} Ry as large as those of the broad resonances. These screening length values are close to the critical screening length of the initial $2p$ state ($\delta^c_{2p} = 4.541a_0$) where its binding energy is very small and, consequently, the overlap of $2p$ wave function with the s-continuum wave is large.

In Fig. 9(c) shown are the cross sections for the $2p \rightarrow \varepsilon d$ photoionization channel for the same screening lengths and for the unscreened case. The well known fact from the photoionization studies for isolated atoms that the cross section for $np \rightarrow \varepsilon d$ channel is about one order of magnitude larger than that for the $np \rightarrow \varepsilon s$ channel is confirmed also in the present screened case. Except for the screened cases with $\delta = 10.7a_0$ and $\delta = 17.1a_0$, the cross section behavior for other screened cases in Fig. 9(c) is typical, being above the cross section of the unscreened case in the photoelectron energy range around the cross section maximum and decreasing at low energies according to the Wigner law (in the present case k^5). The resonance behavior of the cross sections for $\delta = 10.7a_0$ and $\delta = 17.1a_0$ at the energies of $\sim 8.66 \times 10^{-4}$ and $\sim 9.27 \times 10^{-5}$ Ry, respectively, is due to the fact that these values of the screening length are in the regions of the quasibound states associated with the critical screening lengths $\delta^c_{3d} = 10.947a_0$ and $\delta^c_{4d} = 17.210a_0$ (Table I).

The total photoionization cross section from the $2p$ state [Fig. 9(a)] obviously reflects the combined features of the $2p \rightarrow \varepsilon s$ and $2p \rightarrow \varepsilon d$ channel cross sections. The minima in the total cross section for $\delta = 7.1a_0$ and $\delta = 12.6a_0$ at $\sim 3 \times 10^{-3}$ and $\sim 4 \times 10^{-4}$ Ry, respectively, can be interpreted, in a broader sense, as Combet-Farnoux minima, although the main role in their appearance plays the broad resonances for these screening lengths in the $2p \rightarrow \varepsilon s$ channel. The small plateau in the $\delta = 8a_0$ total cross section around the photoelectron energy of $\sim 10^{-3}$ Ry is a trace of a proper Combet-Farnoux minimum as well.

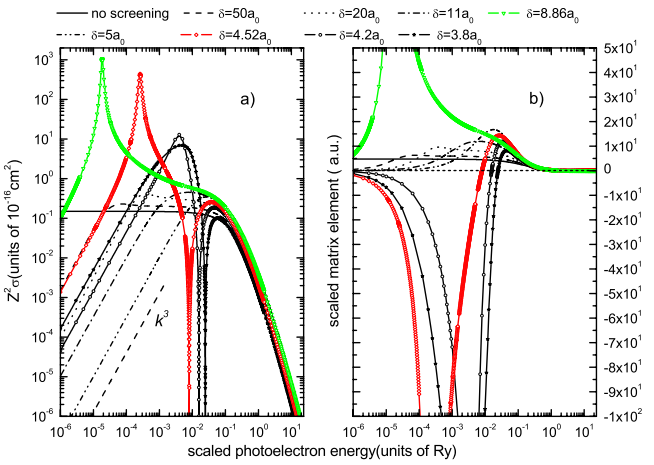

FIG. 11. (Color online) (a) Scaled photoionization cross sections for the $2s$ state as a function of the scaled photoelectron energy for the pure Coulomb case and for the screened case with scaled screening lengths $\delta = 50a_0$, $20a_0$, $11a_0$, $8.86a_0$, $5a_0$, $4.52a_0$, $4.2a_0$, $3.8a_0$. Panel (b): dipole matrix elements.

In Fig. 10 we present the energy dependence of total photoionization cross sections for the $3d$ state [panel (a)], the $3d \rightarrow \varepsilon p$, and $3d \rightarrow \varepsilon f$ cross sections [panels (b) and (c), respectively], for the unscreened case and for the screened cases, with $\delta = 50a_0, 28.2a_0, 22a_0, 20a_0, 14.6a_0, 12.0a_0$. The critical screening length of the $3d$ bound state is $\delta^c_{3d} = 10.947a_0$. An important new element to be noted in these figures is the appearance of shape resonances in the $3d \rightarrow \varepsilon p$ cross section [Fig. 10(b)] for the screening length values $\delta = 14.6a_0$ and $\delta = 22.0a_0$ at the photoelectron energies of $\sim 4.44 \times 10^{-5}$ and $\sim 1.36 \times 10^{-5}$ Ry, respectively. Shape resonances in the $l \rightarrow l-1$ transitions have rarely been observed in the isolated atom photoionization cross sections. These screening lengths are slightly below the critical screening lengths of $4p$ and $5p$ bound states ($\delta^c_{4p} = 14.731a_0$, $\delta^c_{5p} = 22.130a_0$) and reflect the existence of quasibound states there. The resonances in Fig. 10(c) for the $3d \rightarrow \varepsilon f$ for $\delta = 20a_0$ (at $\varepsilon \sim 8.79 \times 10^{-5}$ Ry) and $\delta = 28.2a_0$ (at $\varepsilon \sim 2.43 \times 10^{-5}$ Ry) are due to the quasibound states in the vicinity of critical screening lengths $\delta^c_{4f} = 20.068a_0$ and $\delta^c_{5f} = 28.257a_0$. All these resonances are observed in the total cross section in Fig. 10(a) as well. Their displacement on the energy scale creates the observed minima in the total photoionization cross section. The plateau in the total cross section for $\delta = 12a_0$ in the energy range of $\sim(1-3) \times 10^{-3}$ Ry is a reflection of a proper Combet-Farnoux minimum.

C. Initial state wave functions with nodes ($n-l-1>0$)

We now present the photoionization cross sections for the $2s$, $3s$, $3p$ states that have one or more nodes.

In Fig. 11 we show the energy dependence of the photo-

ionization cross sections [panel (a)] and dipole matrix elements [panel (b)] for the $2s$ initial state in the pure Coulomb interaction case and for the screened cases with Debye lengths $\delta=50a_0, 20a_0, 11a_0, 8.86a_0, 5a_0, 4.52a_0, 4.2a_0, 3.8a_0$. The most remarkable feature in Fig. 11(a), besides the four resonances at lower energies, is the minima in the cross sections for $\delta=4.52a_0$, $4.2a_0$, and $3.8a_0$ in the energy range $\varepsilon \sim (0.8-2.5)\times 10^{-2}$ Ry. These are the Cooper minima, associated with the zeroes of the $2s\rightarrow \varepsilon p$ matrix element for these values of δ and for well defined energies in the above range, as shown in the inset of Fig. 11(b). It should be noted that each of these minima is preceded on the energy scale by a resonance corresponding to the same value of δ. The resonances for $\delta=4.52a_0$, $4.2a_0$, and $3.8a_0$ are associated with the quasibound states that appear when the $2p$ bound state emerges in the continuum at $\delta^c_{2p}=4.541a_0$. These quasibound states have the same nodal structure as the initial $2s$ state. As we have argued earlier, when δ varies in the resonant region the position of the resonance varies as well: the larger the difference $\delta^c_{2p}-\delta$ is the smaller the resonance peak is and the larger the energy is at which it appears. Consequently, the Cooper minima associated with these resonances also move to larger energies with decreasing δ below δ^c_{2p}, as observed in Fig. 11(a). The moving of the Cooper minimum in Fig. 11(a) to higher energies when δ decreases below δ^c_{2p} (or, equivalently, the moving of the zero of the $2s-\varepsilon p$ dipole matrix element) can be easily understood from the variation of the p-phase shift Δ_p when δ varies. From Fig. 7(b) we see that when δ $(<\delta^c_{2p})$ decreases, the phase shift Δ_p also decreases. In order to keep the zero of the $2s-\varepsilon p$ matrix element unchanged, the argument of the continuum p-wave function must not change, which requires increase of the wave number to compensate for the decrease of Δ_p when δ decreases. The connection of the Cooper minima with the shape resonances has also been previously discussed in the isolated multielectron atom case [40] and terms of the change of the phase shift near the top of the centrifugal barrier.

Within the present picture of association of the Cooper minima with the shape resonances whose quasibound states have the same nodal structure as the initial bound state, the appearance of "multiple" Cooper minima seen in Fig. 11(a) looks quite natural. In fact, as we shall see later in other examples, when δ continuously decreases in the resonant region $\delta_0(l)\leq\delta\leq\delta^c_{nl}$ the phase shift of the $(l+1)$th wave will also smoothly decrease [see Fig. 7(b) for the particular case of the p wave] and the dipole matrix element for the $l\rightarrow l+1$ transition can be kept zero by appropriately increasing the wave number $k=(2\varepsilon)^{1/2}$. Therefore, the Cooper minima form a continuum over the $\delta_0(l)\leq\delta\leq\delta^c_{nl}$ range of δ and a corresponding photoelectron energy range.

Multiple Cooper minima have been seen in the $l\rightarrow l+1$ photoionization channel cross sections of excited Cs($5d$) [41] (two minima) and Cs($9d$) [42] (three minima) calculated in one-particle approximation with Hartree-Slater central-field potential however without clear association with shape resonances. Two minima in the photoionization cross sections of Cs(nd) $(n=5,9,11)$ were also found in Ref. [43] by using the Hartee-Fock potential and the random phase approximation with exchange (RPAE). It was demonstrated in this work

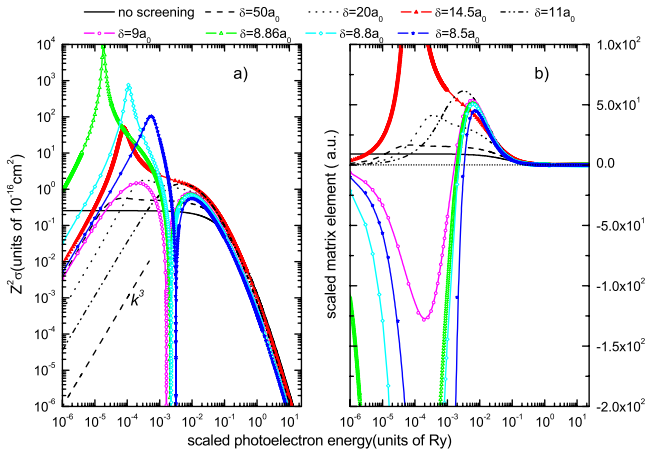

FIG. 12. (Color online) (a) Scaled photoionization cross sections for the $3s$ state as a function of scaled photoelectron energy for the pure Coulomb case and for the screened case with scaled screening lengths $\delta=50a_0, 20a_0, 14.5a_0, 11a_0, 9a_0, 8.86a_0, 8.8a_0, 8.5a_0$. Panel (b): dipole matrix elements.

that the number, the shape, and the energy position of the Cooper minima are highly sensitive to the approximation in which the calculations are performed.

The cross section for $\delta=8.86a_0$ in Fig. 11(a) also exhibits a resonance at $\varepsilon\simeq 2\times 10^{-5}$ Ry associated with the quasibound states for δ below $\delta^c_{3p}=8.873a_0$. The $2s-\varepsilon p$ matrix element in this case, however, does not have a zero [see Fig. 11(b)] and the resonance is not followed by a Cooper minimum in the cross section. It should be remarked that the quasibound states formed in the region $\delta\leq\delta^c_{3p}$ do not have the same nodal structure as the initial $2s$ state and so does the temporarily captured p wave whose phase shift is now increased by π radians with respect to the $\delta\leq\delta^c_{2p}$ values. This makes the matrix element to be positive.

The $3s\rightarrow\varepsilon p$ photoionization cross sections for the unscreened and screened cases with

$$\delta=50a_0, 20a_0, 14.5a_0, 11a_0, 9a_0, 8.86a_0, 8.8a_0, 8.5a_0$$

are shown in Fig. 12 [panel (a)] together with the corresponding dipole matrix elements [panel (b)]. The resonances for $\delta=8.86a_0, 8.8a_0, 8.5a_0$ and associated with them Cooper minima are related to the quasibound states of the $3p$ state entering the continuum at $\delta^c_{3p}=8.872a_0$. The resonance for $\delta=14.5a_0$ is related to the quasibound states of the $4p$ state $(\delta^c_{4p}=14.731a_0)$. The only new feature to be noted in Fig. 12(a) that is not present in Fig. 11(a) is the Cooper minimum for $\delta=9a_0$ at $\varepsilon\simeq 1.8\times 10^{-3}$ Ry. The value $\delta=9a_0$ lies slightly above δ^c_{3p}, i.e., outside the region of $3p$ quasibound states. This Cooper minimum is of the type commonly appearing in the isolated multielectron atomic systems and its appearance can be related to the change of the p-wave phase shift near the top of the centrifugal barrier [20–22,37–40]. However, the fact that it appears for a screening length just before the $3p$ state enters the continuum deserves further investigation, as similar Cooper minima appear in other $l\rightarrow l+1$ cross sections (see next figure).

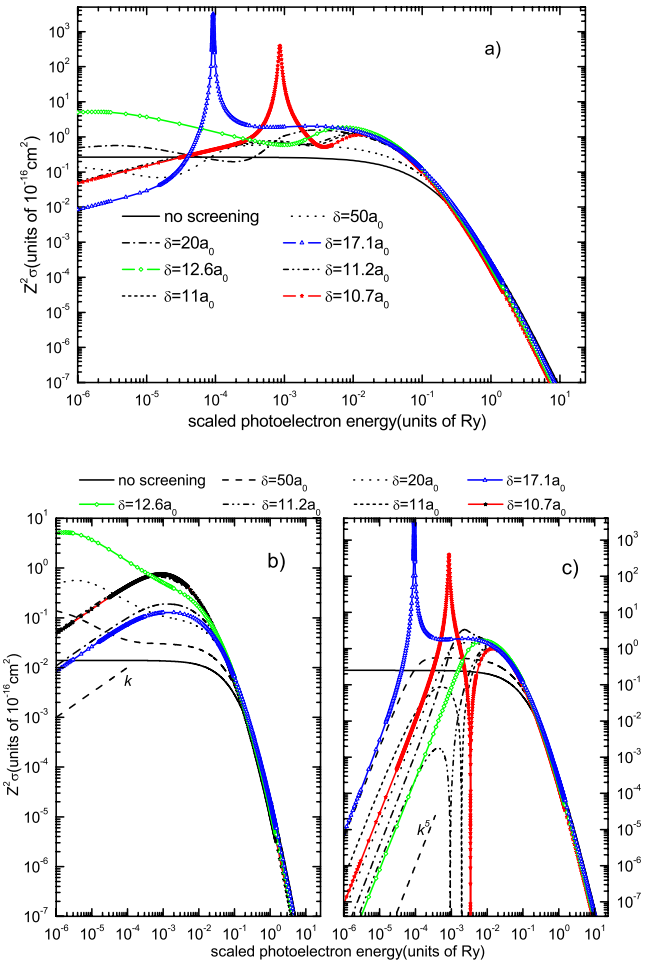

FIG. 13. (Color online) Scaled photoionization cross sections for $3p$ state as a function of the scaled photoelectron energy for the pure Coulomb case and for the screened case with scaled screening lengths $\delta=50a_0, 20a_0, 17.1a_0, 12.6a_0, 11.2a_0, 11a_0, 10.7a_0$. Panel (a): total cross sections; panels (b) and (c): cross sections for the $3p\rightarrow\varepsilon s$ and $3p\rightarrow\varepsilon d$ channels, respectively.

The total, $3p\rightarrow\varepsilon s$ and $3p\rightarrow\varepsilon d$, photoionization cross sections for the unscreened and screened cases with $\delta=50a_0, 20a_0, 17.1a_0, 12.6a_0, 11.2a_0, 11a_0, 10.7a_0$ are displayed in Fig. 13 [panels (a)–(c)], respectively. The cross sections for the $3p\rightarrow\varepsilon s$ photoionization channel [Fig. 13(b)] show a very similar energy behavior as those for the $2p\rightarrow\varepsilon s$ transition in Fig. 9(b). The broad low-energy resonances of the cross sections for $\delta=50a_0$, $20a_0$, and $12.6a_0$ are due to the closeness of these screening lengths to the critical screening lengths of the bound states $8s$ ($\delta^c_{8s}=50.44a_0$ [30]), $5s$, and $4s$ [$\delta^c_{5s}=19.772a_0$, $\delta^c_{4s}=12.687a_0$ (Table I)], respectively, as discussed in Sec. III B. The cross sections for the $3p\rightarrow\varepsilon d$ photoionization channel [Fig. 13(c)] for $\delta=10.7a_0$ and $\delta=17.1a_0$ exhibit resonances at $\varepsilon\sim1\times10^{-3}$ Ry and $\varepsilon\sim1\times10^{-4}$ Ry, respectively, associated with the quasibound $3d$ and $4d$ states in the continuum ($\delta^c_{3d}=10.947a_0$, $\delta^c_{4d}=17.210a_0$). For the reasons discussed above, the resonance for $\delta=10.7a_0$ is followed by a Cooper minimum (at $\varepsilon\simeq3.2\times10^{-3}$ Ry), while that for $\delta=17.1a_0$ is not. Cooper minima are present, however, also in the cross sections for $\delta=11a_0$ (at $\varepsilon\simeq2\times10^{-3}$ Ry) and $\delta=11.2a_0$ (at $\varepsilon\simeq1\times10^{-3}$ Ry) which are slightly larger than the critical screening length δ^c_{3d} (i.e., outside the δ region of quasibound $3d$ states). It should be noted that for these values of the screening length the binding energy of the $3d$ state is very small and its diffuse wave function has a large overlap with the continuum. It is obvious that when δ increases continuously in the region $\delta^c_{3d}\leq\delta\leq\delta^t$, the position of the Cooper minimum will also move continuously in the direction of smaller photoelectron energies and at $\delta=\delta^t$ it will reach the threshold. In fact, the continuum of the Copper minima associated with the shape resonances in the region $\delta_0(l)\leq\delta\leq\delta^c_{nl}$ and that of the Cooper minima in the region $\delta^c_{nl}\leq\delta\leq\delta^t_{nl}$ for the $l\rightarrow l+1$ transitions smoothly join at $\delta=\delta^c_{nl}$, as shown in Fig. 14 for the $2p$, $3p$, $3d$, and $4f$ initial states. For $\delta=\delta^c_{nl}$, the shape resonance and its associated Cooper minimum appear at the same photoelectron energy. The values of screening lengths δ^t_{nl} at which the Cooper minimum appears at the threshold for the transitions $2s\rightarrow\varepsilon p$, $3s\rightarrow\varepsilon p$, $3p\rightarrow\varepsilon d$, and $4d\rightarrow\varepsilon f$ are $4.846a_0$, $9.454a_0$, $11.386a_0$, and $20.607a_0$, respectively (cf. Fig. 14).

It is worthwhile to note that the Cooper minima in the $3p\rightarrow\varepsilon d$ channel do not show up in the total $3p$ photoionization cross section [Fig. 13(a)] due to the large values of $3p\rightarrow\varepsilon s$ channel cross sections at the energy positions of these minima.

The shape resonances observed in the considered photoionization channel cross sections for the selected screening lengths can all be represented by the Breit-Wigner formula [17,36]

$$\sigma_r=\sigma_0\frac{(\Gamma/2)^2}{(E-E_r)^2+(\Gamma/2)^2}, \tag{20}$$

where the values of their energy position (E_r) and width (Γ) are given in Table IV.

We have performed cross section calculations also for the $4d\rightarrow\varepsilon p$, $4d\rightarrow\varepsilon f$ photoionization channels hoping to find Cooper minima also in the $4d\rightarrow\varepsilon p$ cross section when δ varies. However, we were unable to find such minima in the $4d\rightarrow\varepsilon p$ photoionization channel. Such minima have been observed in the Cs($5d\rightarrow\varepsilon p$) [41], Cs($9d\rightarrow\varepsilon p$) [42], and Cs($nd$) ($n=5,9,11$) [43] photoionization cross section calculations performed within the independent particle approximation with a Hartree-Slater central potential [41,42] and the RPAE [43], respectively. The appearance of Cooper minima in isolated excited atomic systems in $l\rightarrow l-1$ photoionization channels and their absence in the case of ground-state atoms and in the Yukawa potential are apparently related to the much stronger screening experienced by the initial state wave function in the later two cases than in the former one.

IV. CONCLUSIONS

In the present work we have performed a systematic study of the dynamics of the photoionization process of a hydrogenlike ion with screened Coulomb interaction in the form of a Debye-Hückel (or Yukawa) potential. (We note that the potential [Eq. (1)] represents the static plasma screening of the charged particle interaction. Only if the ion velocity is

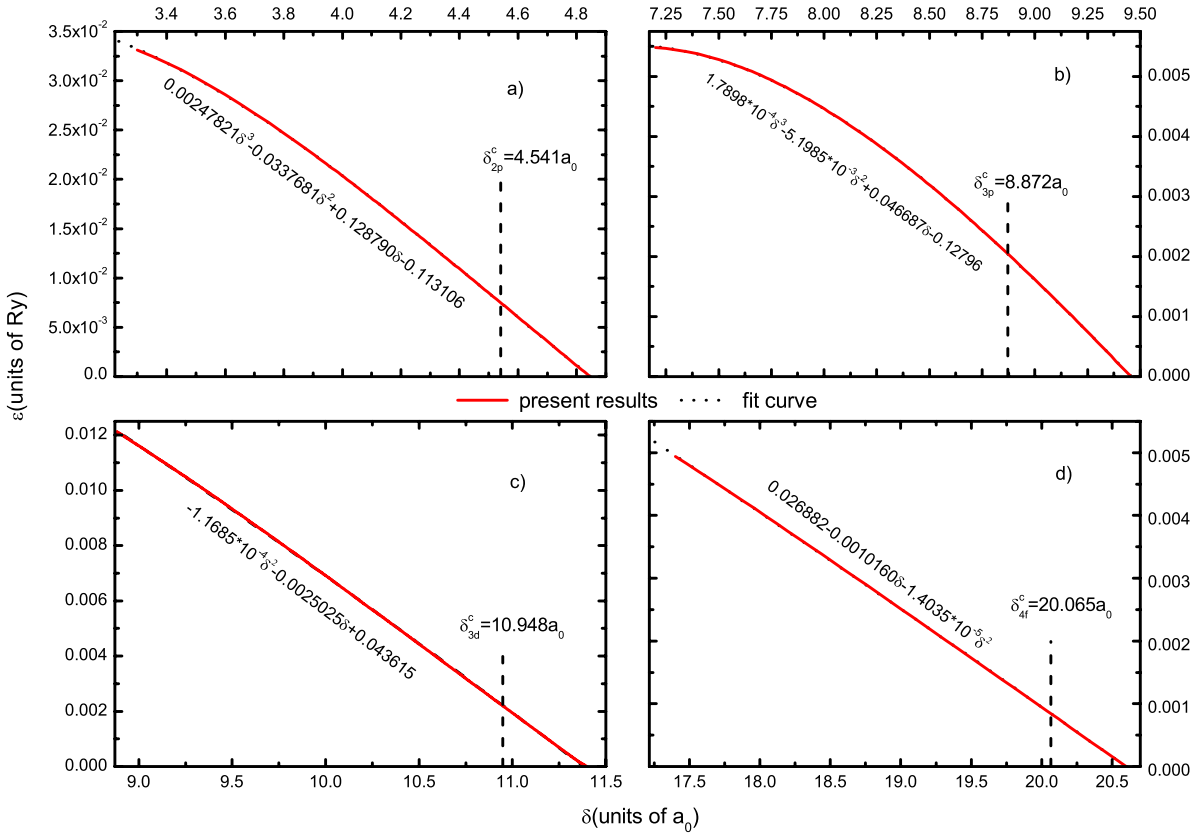

FIG. 14. (Color online) Cooper minima in the $n,l\rightarrow\varepsilon,l+1$ photoionization cross section as the function of the screening length. Panel (a): $2s\rightarrow\varepsilon p$; panel (b): $3s\rightarrow\varepsilon p$; panel (c): $3p\rightarrow\varepsilon d$; and panel (d): $4d\rightarrow\varepsilon f$.

comparable or higher than the thermal plasma electron velocity dynamical plasma screening effects in the electron-ion interaction appear [44]. In the Debye plasmas with close electron and ion temperatures the effect of dynamical screening is of the order of electron–ion mass ratio.)

The presence of a smoothly varying parameter in the potential (the screening strength or, its inverse equivalent, the Debye length) has allowed us to investigate the dynamics of the process in a much more transparent way than it is possible in the isolated atoms or ions. In the isolated atom (ion) case the electron screening of the nuclear Coulomb potential is irregular when increasing the atomic number due to the well-known peculiarities in the filling of electronic subshells when the nuclear charge increases. We have found that the most important role in the photoionization dynamics plays the emergence of the discrete nl states in the continuum for certain critical screening lengths, δ_{nl}^{c}, and the associated appearance of quasibound (for $l>0$) or virtual (for $l=0$) states in the neighborhood of δ_{nl}^{c}, responsible for the shape and broad resonances in the photoionization cross sections. The appearance of the Cooper minima is also closely related to these critical values of the screening length (see Sec. III C and Fig. 14), but this connection has still not been established in a clear and transparent way. We have found that for the $nl\rightarrow\varepsilon l'$ photoionization channel, series (or a continuum) of shape resonances appear for $\delta\leq\delta_{n'l'}^{c}$ for $n'\geq n$ and $l'=l\pm1$ $(l'>0)$, the most pronounced of which in the cross section are those with $n'=n$, $l'=l+1$. In this $(n'=n,\ l'=l+1)$ case each shape resonance is accompanied by a Cooper minimum, i.e., the resonance in the cross section smoothly goes over into a Cooper minimum with increasing (sometimes slightly) the energy (see Figs. 11–13). The resonance series associated with the critical screening lengths of the states having $n'>n$ are not followed by Cooper minima. Another continuum of Cooper minima attached to the critical screening length $\delta_{n,l+1}^{c}$ appears in the region of Debye lengths $\delta_{n,l+1}^{t}\geq\delta\geq\delta_{n,l+1}^{c}$ which terminates at the threshold. Present calculations have also demonstrated the other properties of a short-range potential: the Wigner threshold law for inelastic processes and the Levinson theorem.

TABLE IV. The energy position E_r and width Γ of the shape resonances for the photoionization cross, E_r and Γ, are in units of Ry. The numbers in parentheses are powers of 10.

Transition	$\delta(a_0)$	E_r (Ry)	Γ (Ry)	σ_0 (10^{-16} cm^2)
$1s\rightarrow\varepsilon p$	4.52	2.58(−4)	5.49(−5)	9.09(2)
	8.86	1.85(−5)	2.99(−6)	1.82(2)
$2p\rightarrow\varepsilon d$	10.70	8.66(−4)	7.09(−5)	1.87(2)
	17.10	9.27(−5)	2.53(−6)	7.70(2)
$3d\rightarrow\varepsilon p$	14.60	4.44(−5)	2.40(−5)	1.25(1)
	22.00	1.36(−5)	6.36(−6)	3.08(0)
$3d\rightarrow\varepsilon f$	20.00	8.79(−5)	1.31(−8)	2.12(6)
	28.20	2.43(−5)	2.58(−9)	1.57(6)

We hope that the results presented here will be of interest in the studies of laboratory and astrophysical plasmas in which the plasma screening of Coulomb interaction can be described by the Debye-Hückel potential. The most important result from the application point of view is the finding that due to the shape and broad low-energy resonances, the photoionization cross section in a Debye plasma can be several orders of magnitude larger than that in the pure Coulomb case for a broad range of photon energies and plasma parameters.

ACKNOWLEDGMENTS

One of us (R.K.J.) is grateful to the Institute of Applied Physics and Computational Mathematics, Beijing, for the warm hospitality during the period when this work was performed. This work has been partially supported by the National Natural Science Foundation of China (Grants No. 10604011, No. 10734140, No. 10875017, and No. 10974021), and the National Key Laboratory of Computational Physics Foundation (Grant No. 9140C6904030808).

[1] D. Salzman, *Atomic Physics in Hot Plasmas* (Oxford University Press, Oxford, 1998).
[2] M. S. Murillo and J. C. Weisheit, Phys. Rep. **302**, 1 (1998).
[3] A. N. Sil, S. Canuto, and P. K. Mukherjee, Adv. Quantum Chem. **58B**, 115 (2009).
[4] J. C. Weisheit and B. W. Shore, Astrophys. J. **194**, 519 (1974).
[5] B. W. Shore, J. Phys. B **8**, 2023 (1975).
[6] F. E. Höhne and R. Zimmermann, J. Phys. B **15**, 2551 (1982).
[7] Y.-D. Jung, Phys. Plasmas **5**, 3781 (1998); **5**, 4456 (1998).
[8] L. B. Zhao and Y. K. Ho, Phys. Plasmas **11**, 1695 (2004).
[9] S. Sahoo and Y. K. Ho, Phys. Plasmas **13**, 063301 (2006); Res. Lett. Physics **2009**, 832413 (2009).
[10] S. Sahoo and Y. K. Ho, J. Quant. Spectrosc. Radiat. Transf. (to be published).
[11] E. P. Wigner, Phys. Rev. **73**, 1002 (1948).
[12] D. R. Bates, Mon. Not. R. Astron. Soc. **106**, 432 (1946).
[13] M. J. Seaton, Proc. R. Soc. London, Ser. A **208**, 418 (1951).
[14] J. W. Cooper, Phys. Rev. **128**, 681 (1962); Phys. Rev. Lett. **13**, 762 (1964).
[15] F. Combet-Farnoux, *Proceedings of the International Conference on Inner Shell Ionization Phenomena* (University of Georgia Press, Atlanta, 1972), Vol. 2, p. 1130.
[16] J. P. Connerade, *Highly Excited Atoms* (Cambridge University Press, Cambridge, 1998), p. 136.
[17] R. G. Newton, *Scattering Theory of Waves and Particles* (McGraw-Hill, New York, 1966).
[18] S. D. Oh and R. H. Pratt, Phys. Rev. A **34**, 2486 (1986).
[19] U. Fano and J. W. Cooper, Rev. Mod. Phys. **40**, 441 (1968).
[20] S. T. Manson and J. W. Cooper, Phys. Rev. **165**, 126 (1968).
[21] S. T. Manson, Phys. Rev. A **31**, 3698 (1985).
[22] X. M. Tong, J. M. Li, and R. H. Pratt, Phys. Rev. A **42**, 5348 (1990).
[23] E. Forest and R. D. Ruth, Physica D **43**, 105 (1990); H. Yoshida, Phys. Lett. A **150**, 262 (1990).
[24] X. S. Liu, X. Y. Liu, Z. Y. Zhou, P. Z. Ling, and S. F. Pan, Int. J. Quantum Chem. **79**, 343 (2000).
[25] Y. Y. Qi, J. G. Wang, and R. K. Janev, Phys. Rev. A **78**, 062511 (2008).
[26] Y. Y. Qi, Y. Wu, J. G. Wang, and Y. Z. Qu, Phys. Plasmas **16**, 023502 (2009).
[27] Y. Y. Qi, Y. Wu, and J. G. Wang, Phys. Plasmas **16**, 033507 (2009).
[28] H. A. Bethe and E. E. Salpeter, *Quantum Mechanics of One- and Two-Electron Atoms* (Academic, New York, 1957).
[29] T. E. Simons, Comput. Chem. (Oxford) **21**, 125 (1997).
[30] F. J. Rogers, H. C. Graboske, and D. J. Harwood, Phys. Rev. A **1**, 1577 (1970).
[31] L. D. Landau and E. M. Lifshitz, *Quantum Mechanics: Non-Relativistic Theory* (Pergamon, London, 1958).
[32] F. Calogero and G. Cozenza, Nuovo Cimento A **45**, 867 (1966).
[33] A. S. Dickinson, J. Phys. B **4**, L116 (1971).
[34] M. Bylicki, A. Stachow, J. Karwowski, and P. K. Mukherjee, Chem. Phys. **331**, 346 (2007).
[35] L. Liu, J. G. Wang, and R. K. Janev, Phys. Rev. A **77**, 042712 (2008).
[36] J. R. Taylor, *Scattering Theory* (Willey, New York, 1971).
[37] S. T. Manson, Phys. Rev. **182**, 97 (1969).
[38] R. Y. Yin and R. H. Pratt, Phys. Rev. A **35**, 1154 (1987).
[39] R. H. Pratt, R. Y. Yin, and X. Liang, Phys. Rev. A **35**, 1450 (1987).
[40] Y. S. Kim, R. H. Pratt, and A. Ron, Phys. Rev. A **24**, 1626 (1981).
[41] A. Msezane and S. T. Manson, Phys. Rev. Lett. **35**, 364 (1975).
[42] J. Lahiri and S. T. Manson, Phys. Rev. Lett. **48**, 614 (1982).
[43] N. B. Avdonina and M. Ya. Amusia, J. Phys. B **16**, L543 (1983).
[44] A. I. Akhiezer, I. A. Akhiezer, R. V. Polovin, A. G. Sitenko, and K. N. Stepanov, *Plasma Electrodynamics*, Non-Linear Theory and Fluctuations Vol. 2 (Pergamon Press, Oxford, 1975).